Available online at www.sciencedirect.com
ScienceDirect
Journal of Computational Physics 227 (2008) 2540–2559
JOURNAL OF COMPUTATIONAL PHYSICS
www.elsevier.com/locate/jcp

Velocity limit in DPD simulations of wall-bounded flows

Dmitry A. Fedosov, Igor V. Pivkin, George Em Karniadakis *

Division of Applied Mathematics, Brown University, Providence, RI 02912, USA

Received 2 January 2007; received in revised form 24 August 2007; accepted 5 November 2007
Available online 19 November 2007

Abstract

Dissipative particle dynamics (DPD) is a relatively new mesoscopic simulation approach, which has been successfully applied in modeling complex fluids in periodic domains. A recent modification [X.J. Fan, N. Phan-Thien, S. Chen, X.H. Wu, T.Y. Ng, Simulating flow of DNA suspension using dissipative particle dynamics, Physics of Fluids 18 (6) (2006) 063102] has allowed DPD simulations of polymers for realistic values of the Schmidt number. However, DPD and its extensions encounter difficulties in simulating even simple fluids in *wall-bounded* domains. The two main problems are wall boundary conditions and compressibility effects – the topic of the present work – which limit the application of DPD to low Reynolds number (*Re*) flows (e.g., $Re < 100$). Here, we establish an empirical criterion that provides an upper limit in velocity and correspondingly in *Re* for a fixed computational domain, assuming a deviation from Navier–Stokes solutions of at most 5%. This limit could be increased by increasing the size of the computational domain at approximately linear computational cost. Results are presented for the lid-driven cavity flow reaching, for first time, $Re = 1000$, and similar extensions can be established for other complex-geometry flows. A systematic investigation is presented with respect to both different types of boundary conditions and compressibility effects for the standard DPD method as well as the modified version that simulates highly viscous fluids.

Keywords: No-slip; Compressibility; Boundary conditions; DPD

1. Introduction

Dissipative particle dynamics (DPD) is a mesoscopic method [2,3] that can potentially bridge the gap between atomistic and continuum descriptions in fluids. The DPD particles represent *clusters* of molecules moving together in a Lagrangian fashion subject to soft quadratic potentials. In contrast to molecular dynamics method, DPD employs much larger time steps and particle sizes because of the soft particle interactions. In particular, the DPD method appears to be successful in simulations of complex fluids, such as suspensions of polymers, DNA, and colloids in a Newtonian incompressible solvent, etc., see [4–6]. Unlike other methods, such as Smoothed Particle Hydrodynamics (SPH) [7] and Lattice Boltzmann Method (LBM) [8], the DPD model includes thermal fluctuations, which may play a crucial role even in mesoscopic flows. Such corrections

* Corresponding author. Tel.: +1 401 863 1217; fax: +1 401 863 3369.
E-mail address: gk@dam.brown.edu (G.E. Karniadakis).

0021-9991/$ - see front matter © 2007 Elsevier Inc. All rights reserved.
doi:10.1016/j.jcp.2007.11.009

have to be explicitly introduced in LBM [9] and SPH [10]. In addition to many simulations of complex fluids, several attempts have been made to simulate simple fluids at *finite* Reynolds number ($Re > 1$ but typicall less than 100) for several prototype flows, e.g. flows past cylinders, spheres, and inside channels and cavities [11–15]. The connection of DPD to molecular dynamics as well as to Navier–Stokes equations was investigated in [16]. It has been found that DPD exhibits hydrodynamic behavior and agrees well with numerical solutions of the Navier–Stokes equations but the question remains when this agreement breaks down and, moreover, what is the level of acceptable accuracy. Unlike continuum-based discretizations where the simulation codes typically blow up for under-resolving a flow field (essentially acting as a diagnostic measure), in the Lagrangian-based DPD simulations there is no blow-up but the simulation may converge to an erroneous flow state – a far more dangerous situation!

An example of a DPD simulation is shown in Fig. 1 for the triangular-cavity flow at Reynolds number $Re = 100$ along with spectral element simulations [17] employing eighth-order polynomials (here, the Reynolds number is based on the lid velocity and the height of the cavity). The figure shows streamlines of the cavity flow with the upper wall moving to the right. In the absence of inertia, the triangular-cavity flow exhibits a cascade of counter-rotating vortices, with their strength decaying exponentially as we approach the bottom corner of the domain (left plot). Hence, capturing these weak secondary vortices is challenging, and, indeed, most standard grid-based methods fail to resolve more than two or three vortices. The effect of inertia appears to modify the flow structure and only two vortices are visible in the spectral element simulations at $Re = 100$ (middle plot). In this case, DPD also resolves two vortices although the secondary vortex appears to be under-resolved. In fact, systematic comparisons between DPD and spectral element solutions showed good agreement of the flow fields at low Re but the results were strongly depended on the boundary conditions employed in DPD to enforce the no-slip condition. At higher values of Re, the DPD results yield relatively large discrepancy compared to the spectral element solutions depending on the specific boundary conditions employed and the velocity of the driven lid.

The problems encountered in the DPD simulation of the triangular-cavity flow are typical in most DPD simulations of wall-bounded flows, namely: (1) the specific implementation of boundary conditions affects the maximum Reynolds number that can be simulated for a specific domain; (2) density fluctuations and associated clustering of particles arise, especially close to walls, which may also affect the bulk of the flow. Compressibility effects are common in other methods (e.g., SPH or LBM) but also different boundary condition models have been shown to greatly affect the flow patterns. These effects have also been identified in [12] as limiting the accuracy of DPD for flows past arrays of spheres and cylinders.

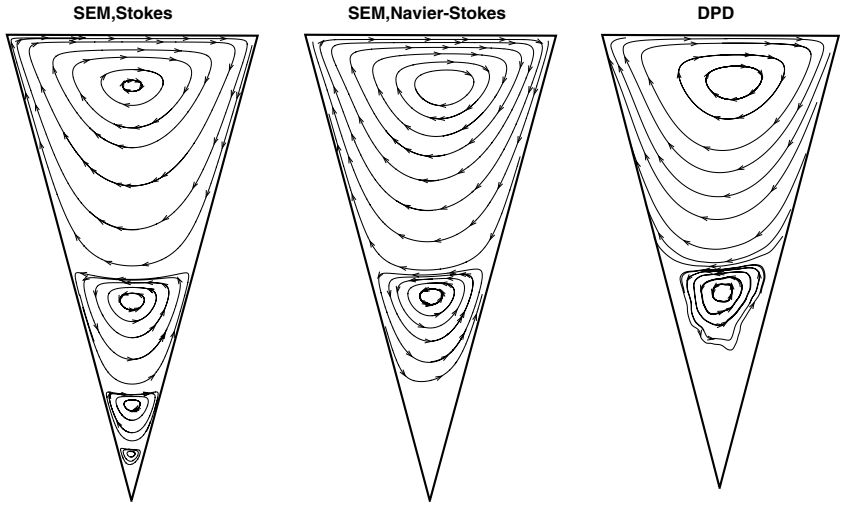

Fig. 1. Streamline patterns from simulations of the triangular-cavity flow. The upper wall is moving to the right and the angle between the two stationary walls is 30°. (left) Stokes flow simulated with spectral elements. (middle) $Re = 100$ flow simulated with spectral elements. (right) $Re = 100$ flow simulated with DPD.

In the current paper, we investigate systematically the aforementioned two issues and develop a simple criterion to diagnose erroneous DPD results in wall-bounded flows. To this end, we consider the square-cavity flow for which there is vast literature of solutions based on discretizations of Navier–Stokes equations. In addition to the standard DPD method, we present results obtained with a modified version of DPD, which was recently introduced in [1]. In this version, the relative dissipative and random force interactions are modified (see Section 2 for details) in order to increase the viscosity of the DPD fluid and hence the Schmidt number, which is defined as $Sc = \frac{\nu}{D}$, where ν is the kinematic viscosity of the fluid and D is the diffusivity. As pointed out in [18], the standard DPD is able to reproduce fluids with values of Schmidt numbers of order $O(1)$, in contrast to $O(10^3)$ Schmidt numbers of real fluids. This increase in Schmidt number is desired in polymer flows and other transport problems.

The paper is organized as follows. In the next section we review briefly the DPD governing equations and in Section 3 we compare various no-slip boundary conditions. In Section 4 we present simulation results for the cavity flow, and subsequently we propose a quantitative criterion (based on the number density) that determines the maximum Reynolds number that can be simulated accurately with DPD. We conclude in Section 5 with a brief discussion.

2. DPD governing equations

The DPD system consists of N point particles of mass m_i, position $\mathbf{r}_i$ and velocity $\mathbf{v}_i$. These particles represent "molecular clusters" rather than individual atoms and interact through simple pairwise-additive forces. The total force exerted on a particle i by particle j consists of three terms: (1) conservative; (2) dissipative; (3) random forces, i.e.,

$$\mathbf{F}_{ij}^{\mathrm{C}} = F_{ij}^{\mathrm{C}}(r_{ij})\hat{\mathbf{r}}_{ij}, \tag{1}$$

$$\mathbf{F}_{ij}^{\mathrm{D}} = -\gamma\omega^{\mathrm{D}}(r_{ij})(\mathbf{v}_{ij}\cdot\hat{\mathbf{r}}_{ij})\hat{\mathbf{r}}_{ij}, \tag{2}$$

$$\mathbf{F}_{ij}^{\mathrm{R}} = \sigma\omega^{\mathrm{R}}(r_{ij})\xi_{ij}\hat{\mathbf{r}}_{ij}, \tag{3}$$

where $\mathbf{r}_{ij} = \mathbf{r}_i - \mathbf{r}_j$, $r_{ij} = |\mathbf{r}_{ij}|$, $\hat{\mathbf{r}}_{ij} = \mathbf{r}_{ij}/r_{ij}$, and $\mathbf{v}_{ij} = \mathbf{v}_i - \mathbf{v}_j$. The coefficients γ and σ determine the amplitude of dissipative and random forces, respectively. ω^{D} and ω^{R} are weight functions, ξ_{ij} is a normally distributed random variable with zero mean, unit variance, and $\xi_{ij} = \xi_{ji}$. All forces act within a sphere of radius r_{c}, the cutoff radius, which defines the length scale in the DPD system. The conservative force $F_{ij}^{\mathrm{C}}(r_{ij})$ is typically given by

$$F_{ij}^{\mathrm{C}}(r_{ij}) = \begin{cases} a_{ij}(1 - r_{ij}/r_{\mathrm{c}}) & \text{for } r_{ij} \leqslant r_{\mathrm{c}}, \\ 0 & \text{for } r_{ij} > r_{\mathrm{c}}, \end{cases} \tag{4}$$

where $a_{ij} = \sqrt{a_i a_j}$ and a_i, a_j are conservative force coefficients for particles i and j, respectively.

The DPD system relaxes to an equilibrium temperature T when the random and dissipative forces satisfy the fluctuation dissipation theorem [19]

$$\omega^{\mathrm{D}}(r_{ij}) = \left[\omega^{\mathrm{R}}(r_{ij})\right]^2, \tag{5}$$

$$\sigma^2 = 2\gamma k_{\mathrm{B}} T, \tag{6}$$

where k_{B} is the Boltzmann constant. The typical choice for the weight functions is

$$\omega^{\mathrm{R}}(r_{ij}) = \begin{cases} (1 - r_{ij}/r_{\mathrm{c}})^p & \text{for } r_{ij} \leqslant r_{\mathrm{c}}, \\ 0 & \text{for } r_{ij} > r_{\mathrm{c}}. \end{cases} \tag{7}$$

where $p = 1$ for the standard DPD method. However, other choices for these envelopes have been proposed in order to increase the Schmidt number of the DPD fluid, e.g., $p = 0.25$ in [1]. We will refer to this version of DPD as "modified DPD" in the current paper.

The time evolution of velocities and positions of particles is described by Newton's second law of motion

$$\mathrm{d}\mathbf{r}_i = \mathbf{v}_i\,\mathrm{d}t, \tag{8}$$

$$\mathrm{d}\mathbf{v}_i = \frac{1}{m_i}\sum_{j\neq i}(\mathbf{F}^{\mathrm{C}}_{ij}\,\mathrm{d}t + \mathbf{F}^{\mathrm{D}}_{ij}\,\mathrm{d}t + \mathbf{F}^{\mathrm{R}}_{ij}\sqrt{\mathrm{d}t}). \tag{9}$$

There are several methods that can be used for the integration of DPD evolution equations. In this work we use two different time-integration algorithms in order to compare their performance in simulations of wall-bounded systems. The selected methods are (1) modified velocity-Verlet algorithm [3], and (2) self-consistent DPD integration scheme [20]. We want to investigate if any of these time-integration algorithms yields results with a different upper limit in *Re*.

3. Boundary conditions

One of the main issues in DPD simulation of wall-bounded flows is the correct imposition of boundary conditions. There are two main approaches for modeling solid boundaries: indirect methods, which avoid direct modeling of the physical boundaries by relying on modifications of the periodic boundary conditions or of the domain [21,22]; and direct methods, which model solid boundaries by locally freezing regions of particles [23,24]. The first category is limited to simple flows, so here we focus on wall boundary conditions in DPD, which employ collections of frozen particles in combination with particle reflection rules. In particular, reflection of fluid particles at the fluid-solid interface prevents fluid particles from penetrating the wall; this can be implemented by using specular, bounce-back, bounce-forward, or Maxwellian reflection.

Here we employ several different (no-slip) wall boundary conditions. Revenga et al. [24] performed simulations of DPD flows without any conservative interactions ($a_{ij} = 0$) and showed that large values of the density of wall particles enforces the no-slip condition at the fluid-solid interface. In [25] the no-slip boundary condition was achieved by employing a bounce-back reflection even for relatively small wall densities. However, in the presence of *repulsive* interactions ($a_{ij} \neq 0$) non-negligible density fluctuations are observed in the near-wall region. More recently, it has been shown [15] that these fluctuations induce an apparent slip – due to the shearing between high and low density layers – and it becomes more pronounced at higher shear rates. Hence, one has to simultaneously impose the no-slip condition directly at the solid boundary and, in addition, to control the near-wall density fluctuations.

Specifically, a force boundary condition (FBC) was developed in [15] by freezing several wall layers of uniformly distributed (simple cubic lattice) DPD particles in combination with bounce-back reflection at the interface. In addition, the repulsive interactions from the wall particles are adjusted according to the fluid and wall number densities, as follows:

$$a_{\mathrm{w}} = \frac{1}{a_{\mathrm{f}}}\left[\frac{0.39(n_{\mathrm{f}}k_{\mathrm{B}}T + 0.1a_{\mathrm{f}}n_{\mathrm{f}}^2)}{0.0303n_{\mathrm{w}}^2 + 0.5617n_{\mathrm{w}} - 0.8536}\right]^2, \tag{10}$$

where a_{w} and a_{f} are the conservative force coefficients of wall and fluid particles, and n_{w}, n_{f} are wall and fluid number densities, respectively. Such tuning of the conservative force does not completely solve the problem of near-wall density fluctuations, however, it eliminates slip for low and moderate shear rates in the standard DPD method (corresponding to $p = 1$ in Eq. (7)).

Results from our various DPD simulations reveal that the problem of density fluctuations close to the wall remains in the case of freezing layers of particles. This artifact is due to an imbalance of the DPD forces between wall particles and surrounding fluid particles along the wall-normal direction. (The dissipative and random forces have no net contributions along the wall-normal direction unlike the conservative force as will be shown at the end of this section.) Therefore, the idea of introducing an *adaptive* wall potential seems to be reasonable, so following [26] we use here two types of adaptive boundary conditions, which we will call *ABC-0* and *ABC-I*. In ABC-0, we freeze several wall layers of DPD particles similar to FBC, but the conservative force of wall particles is set to zero. In order to compensate the repulsive force imbalance from the wall we introduce adaptively a wall force acting on the fluid particles. The adaptive force calculation, which is

described in detail in [26], controls the density fluctuations and can enforce *any* desirable density profile close to the wall. In ABC-I, density fluctuations are controlled similar to ABC-0. However, instead of layers of frozen DPD particles, we introduce image particles in the wall region as it was done in [13,26]. For completeness, we describe below the procedure for computing the random and dissipative force contributions for ABC-I.

Let us consider a wall perpendicular to y-axis and located at $y = y_W$; the wall is moving with velocity $\mathbf{v}_W$ remaining on the $y = y_W$ plane. We assume that there are N_W fluid particles within the cutoff distance r_c from the wall. The ith particle has coordinates (x_i, y_i, z_i) and velocity $\mathbf{v}_i$ while the total force acting on particle i is $\mathbf{F}_i$. It is convenient to introduce a ghost particle g, although it is not necessary to construct it explicitly in the code. The dissipative and random force contributions of the wall boundary conditions at each time step are expressed using the following pseudo-code:

```
for particle i = 1, .., N_W
  create ghost particle g with x_g = x_i + ξ_x, y_g = 2y_W − y_i, z_g = z_i + ξ_z and v_g = 2v_W − v_i.
  for particle j = i + 1, .., N_W
    compute F^R_jg, F^D_jg
    F_j = F_j + F^D_jg + dt^{-1/2} F^R_jg
    F_i = F_i − F^D_jg − dt^{-1/2} F^R_jg
  end
end
```

The random variables ξ_x and ξ_z are uniformly distributed in the interval $[-r_c, r_c]$. In addition, when fluid particles penetrate into the wall region, we perform a bounce-back reflection of these particles into the fluid region.

In the current work, we target uniform density profiles, i.e., the near wall density is equal to the bulk density. We have found that for a uniform density profile close to the wall the iterative adaptive procedure for the conservative force in ABC converges to the wall force that corresponds to a potential profile, which compensates for the imbalance of repulsive forces from the surrounding semi-spherical fluid region. We have verified that the same potential can be obtained by numerical integration of the conservative force multiplied by the radial distribution function over the semi-spherical fluid region – an approach first presented in [27] – i.e.,

$$F_w(h) = n \int_{V_s \setminus V_{cap}(h)} F_w^C(r) g(r)\, dV, \tag{11}$$

where h is the distance from the fluid particle to the wall, n is the number density, V_s is the sphere volume, $V_{cap}(h)$ is a spherical cap (cut out) from the wall, $F_w^C(r)$ is the conservative DPD force in the direction normal to the wall, and $g(r)$ is the radial distribution function. The expression for $F_w(h)$ cannot be obtained analytically because the radial distribution function does not, in general, have an analytical expression. Hence, for a uniform density profile the wall adaptive force can be imposed during the simulation by either using an iterative procedure or by numerical integration after computing the radial distribution function for a specific DPD fluid.

An alternative way to impose the no-slip boundary condition (based on frozen wall particles) is to consider in a pre-processing stage a flow simulation at the equilibrium state (no net fluid motion) in combination with an adaptive wall shear procedure. At the pre-processing stage, the domain – which covers both fluid and solid wall regions – is assumed to be periodic in all directions and without any solid walls present. The DPD particles are distributed in a lattice or randomly in the domain and simulations are run until the equilibrium state is reached. The particles, which occupy the region of solid walls, are then frozen at some instant of time and later used to model solid walls in combination with bounce-back reflection at the fluid-solid interface. We have developed a procedure with two types of boundary conditions, which we denote as EBC-0 when the adaptive wall shear procedure is *not* used and EBC-S when the adaptive procedure is employed.

The details of EBC-S type can be explained using the sketch of Fig. 2. In simulations, we consider subregions of the computational domain of width $L = r_c$ adjacent to the fluid-solid interface in both fluid and wall

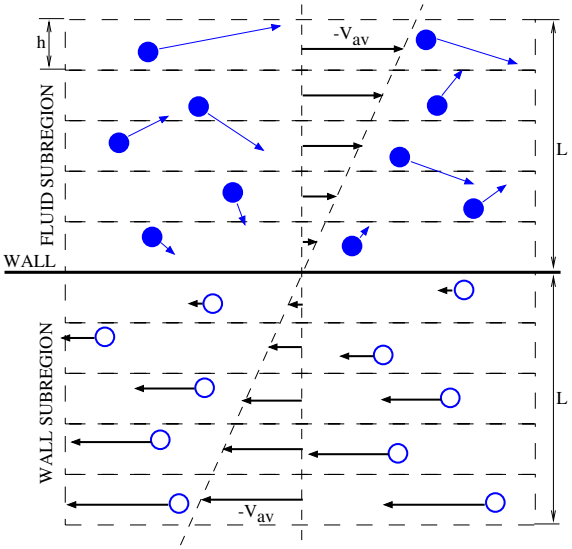

Fig. 2. Sketch illustrating the concept of equilibrium boundary condition with shear (EBC-S).

regions. We divide the fluid and wall subregions into bins of height h, whose value can be chosen based on the desired accuracy of the near-wall velocity profile. These subregions can be divided into bins along the wall if the velocity profile changes in the direction parallel to the wall. During the simulation, in each bin in the fluid subregion the time-averaged velocity $\mathbf{v}_{av}$ is collected over a specified number of time-steps. The velocities of the particles inside each bin in the wall subregion are set to be opposite, i.e. $-\mathbf{v}_{av}$, to the average velocity in the corresponding fluid subregion bin, which is symmetric with respect to the fluid-solid interface. The wall particles (shown as open circles) do not move in the simulations and carry only velocity information, which is used in the calculation of the dissipative force. We find that this model enforces the no-slip boundary conditions and eliminates density fluctuations in the near-wall region, *similarly* to ABC-I. Moreover, the EBC-S model has about the same computational cost as the two previous models (FBC and ABC) and it can be easily implemented.

In summary, all three types of boundary conditions (i.e., FBC, ABC and EBC, see Table 1) are effective for flows involving low to moderate wall shear rates. However, in the high shear rate regime only ABC-I and EBC-S enforce properly the no-slip condition at the walls with minimum near-wall density fluctuations.

3.1. Modified DPD: more viscous fluids

In the discussion so far we have considered the standard DPD method, which simulates fluids with Schmidt number of order one [3]. In a recent paper [1], an attempt was made to achieve much larger values of the Schmidt number and one of the modifications proposed was a change of the weight function of dissipative and random forces. In particular, a slower decay with distance of the interaction envelope enhances the dissipative interactions of particles with surrounding particles and substantially increases the viscosity of the fluid and hence the corresponding Schmidt number. In addition, in order to increase the value of viscosity we can

Table 1
Summary of no-slip wall boundary conditions

FBC	Force boundary condition, Eq. (10)
ABC-0	Adaptive boundary condition with frozen particles
ABC-I	Adaptive boundary condition with image particles
EBC-0	Equilibrium boundary condition without shear correction
EBC-S	Equilibrium boundary condition with shear correction

increase the cutoff radius in the DPD simulation. Here, we are interested to examine how accurate are the three aforementioned types of boundary conditions for the modified DPD method.

To this end, we performed several DPD simulations of Poiseuille flow in a channel. In the case of the *standard DPD* method all types of boundary conditions give correct results for modest levels of wall shear stress. In the *modified DPD* simulations we employed the following parameters: number density $n = 4$; force coefficients $a = 18.75, \gamma = 4.5, \sigma = 3.0$; temperature $k_B T = 1.0$; cutoff radius $r_c = 1.0$; domain size $20 \times 20 \times 10$; pressure drop $g = 0.05$; and exponent in the random force weight function $p = 0.25$ (Eq. (7)). For comparison, the viscosity in the modified DPD simulations is approximately *twice* the viscosity of the standard DPD case while the Schmidt number is about *six* times larger. Fig. 3 summarizes the results from modified DPD simulations. The solution corresponding to ABC-I and EBC-S coincides with the analytical solution. However, in the absence of the adaptive shear procedure, i.e., case EBC-0, we obtain a solution with a small slip at the wall. Also, for simulations employing FBC and ABC-0 we observe an under-development of the Poiseuille profile.

To understand these results we consider each DPD force contribution from the wall separately for the three directional components: normal, streamwise tangential and across-stream tangential. First, we compute them for an ideal implementation of the wall using the periodic Poiseuille flow method (PPFM) [22]. In this method the domain is subdivided into two subdomains and two counter-flowing Poiseuille flows are established by applying a force with the same magnitude but opposite direction in each subdomain. The planes separating the subdomains can be considered as imaginary ideal walls, i.e., walls that are modeled without explicit implementation of the no-slip conditions. At each time step we measure the instantaneous force acting on the particles within distance r from these ideal walls on one side from the particles on the opposite side. We find that only two components of force contributions out of nine have a non-zero *average* value, i.e., the normal component of the conservative force and the streamwise (tangential) component of the dissipative force. They are shown as a function of distance from the wall with solid lines in Fig. 4. The *normal* component of the conservative force acting on the fluid particles from the wall controls the fluid density fluctuations close to the wall. The *streamwise* dissipative force component determines the streamwise velocity profile close to the wall. In the same figure, we plot the *average* values of the forces acting on fluid particles from the wall for different implementations of the wall boundary conditions considered above. We observe that the average values of the normal component of the conservative force are close to the ideal profile for all methods except for FBC. Specifically, FBC leads to results with large density fluctuations compared to other methods (see Fig. 3). The average streamwise dissipative force components of the ABC-I and EBC-S capture the ideal profile quite

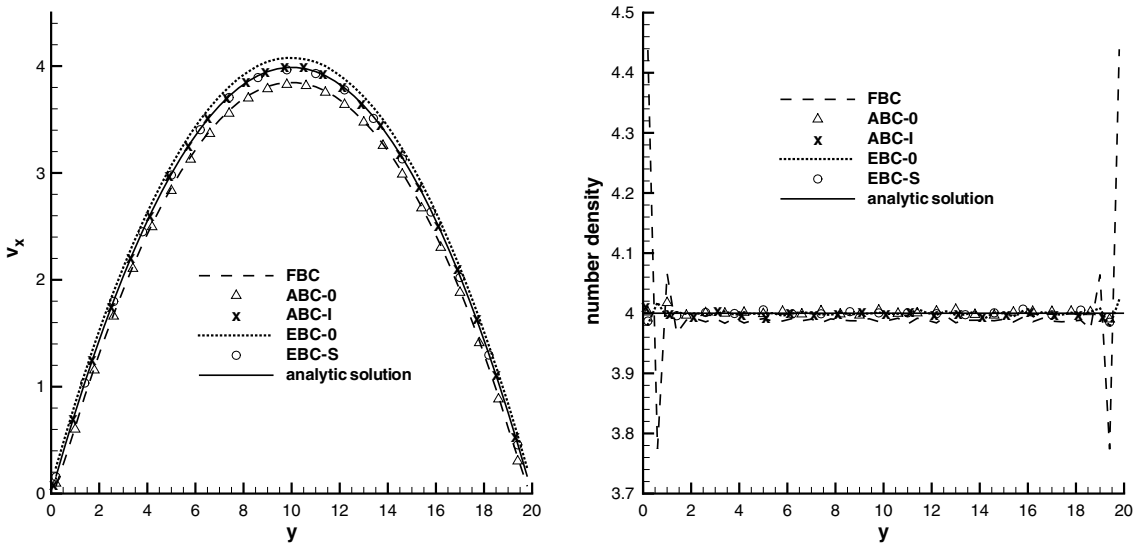

Fig. 3. Modified DPD ($p = 0.25$): comparison of different boundary conditions. (left) Velocity profiles. (right) Density profiles. Only ABC-I and EBC-S give correct results.

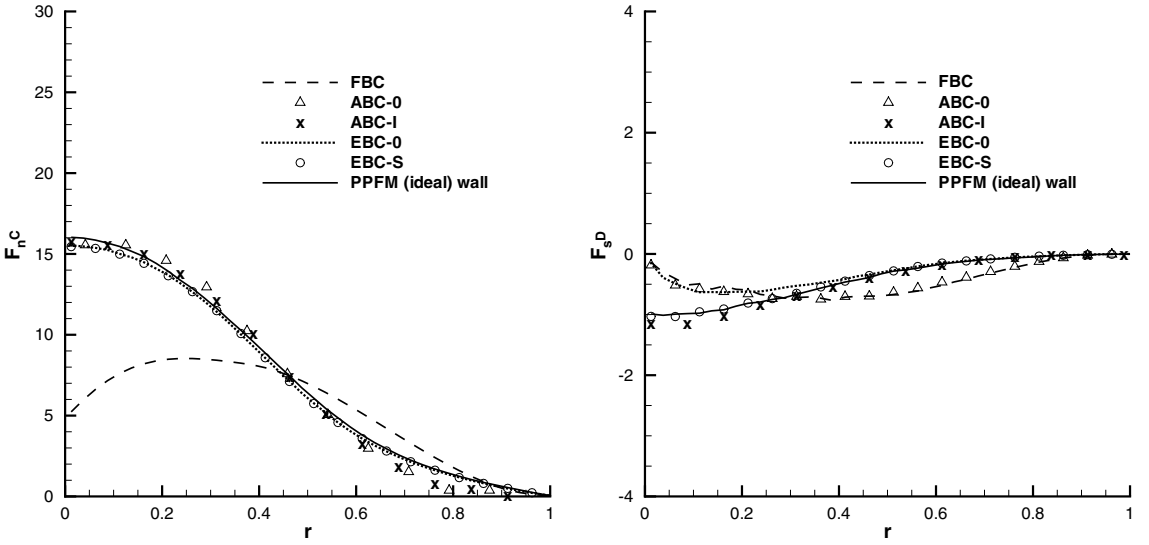

Fig. 4. Average wall forces acting on the fluid particles for different implementations of wall boundary conditions as a function of distance from the wall. (left) Normal component of the conservative force. (right) Streamwise component of the dissipative force.

well. For other methods we observe deviations, which are consistent with the simulation results for the velocity profiles shown in Fig. 3.

4. Simulation results

In this section we present results from DPD simulations of the square lid-driven cavity flow at different Reynolds numbers; the Reynolds number is defined as $Re = \frac{UL}{\nu}$, where U is the velocity of the moving lid, L is the height of the cavity, and ν is a kinematic viscosity of the fluid. The DPD simulation results will be compared to numerical solutions obtained by the highly accurate spectral element discretization of the Navier–Stokes equations [17]. All DPD simulations were performed using the modified version of the velocity-Verlet algorithm [3] for the integration of equations of motion. For comparison purposes, we also employed the self-consistent DPD algorithm [20]; the difference in the results was negligible, i.e., of the order of the statistical fluctuations.

4.1. Simulation parameters

The following parameters are used in DPD simulations. The fluid number density is $n = 3$ and the cutoff radius $r_c = 1$. The conservative force coefficient of fluid particles is $a = 25.0$ while the random and dissipative force coefficients are $\sigma = 3.0$ and $\gamma = 4.5$. The temperature is set to $k_B T = 1$ satisfying the fluctuation–dissipation relations (5) and (6). The kinematic viscosity ν of the DPD fluid is equal to 0.2854; it was obtained by fitting a parabola to the DPD results from periodic Poiseuille flow method (PPFM) described in [22]. The majority of simulations employed the modified velocity-Verlet integration scheme with $\lambda = 0.5$ [3], which corresponds to the standard velocity-Verlet scheme widely used in Molecular Dynamics simulations. The time step is between 0.001 and 0.01 depending on the Reynolds number of a particular case. With regards to boundary conditions, for FBC and ABC-0 the solid walls are modeled by freezing several layers of uniformly distributed DPD particles. The number density of the walls is $n_w = 8.6$ while the conservative force coefficient of wall particles is $a_w = 0.1017$ according to Eq. (10) [15]. For EBC-0 and EBC-S the solid walls are modeled by freezing DPD particles at equilibrium while the density of the walls is the same as that of fluid. For ABC-0 and ABC-I we use a $5 \times 1 \times 1$ bin grid for all walls in order to compute the density fluctuations. In particular, the bins have the length of the cavity wall and height $\frac{r_c}{5} = 0.2$. We are targeting uniform density profile with

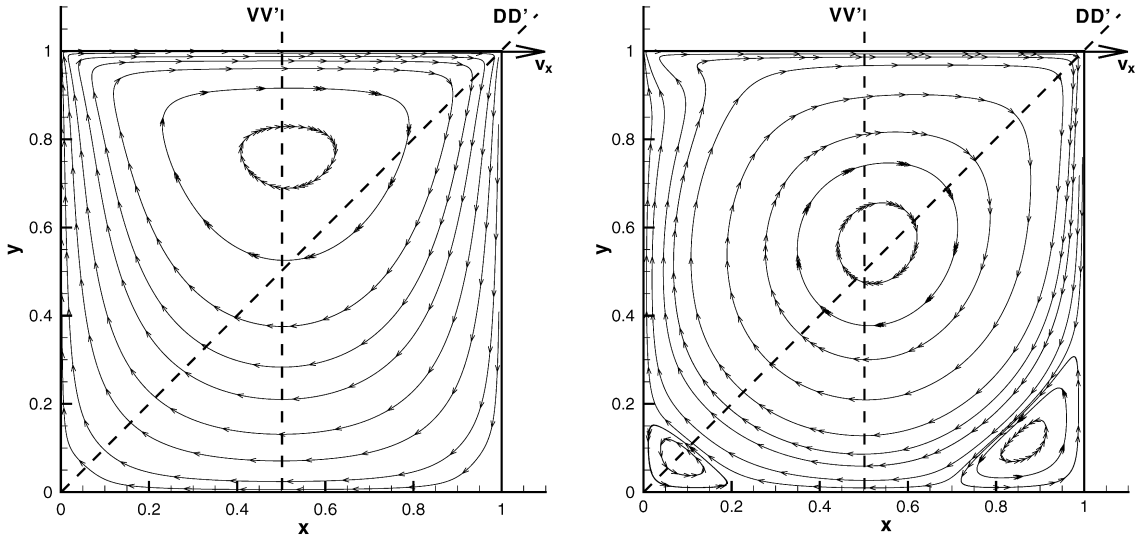

Fig. 5. Streamline pattern obtained using spectral element discretizations at (left) $Re = 10$ and (right) $Re = 1000$. The upper wall is moving to the right. Comparison of results is performed along the cuts VV′ and DD′. The coordinates are normalized by the domain size.

density magnitude $n = 3$. In each corner we have two overlapping grids, which result in non-uniform density profile in the corner as we will observe later. For EBC-S we use a $5 \times 5 \times 1$ bin grid for all walls in order to compute the near-wall velocity profile and mimic a counter flow in the wall region. In addition, we employed a bounce-back reflection at the fluid-solid interface. For comparison, we have run several cases with specular and Maxwellian reflection; the results showed no dependence on the particular reflection type.

The flow domain size is $10 \times 10 \times 1000$ (in DPD units), and it is periodic in the z direction. Another set of DPD simulations was performed on a larger domain, corresponding to $20 \times 20 \times 500$ (in DPD units). The large domain size in the z direction allowed us to obtain converged statistics relatively quickly after the steady state was reached. The domain is subdivided into 40 bins in x and y directions. The simulations are run for $500,000$ time steps and statistical data are collected starting from time step 50,000. The highest Reynolds number in the current study, $Re = 1000$, was obtained on a domain $100 \times 100 \times 10$.

4.2. Reference numerical solution

In Fig. 5 we show streamlines for the square-cavity flow at Reynolds number $Re = 10$ and $Re = 1000$. The solution was obtained using the solver NEKTAR [17] based on spectral element discretization of the incompressible Navier–Stokes equations using 900 quadrilateral elements with fourth- and sixth-order polynomials, for the low and high Reynolds numbers, respectively. The velocity of the upper wall is fixed while no-slip conditions are applied at all the other walls.

4.3. Low reynolds number flow

We start our DPD tests from the case of static fluid corresponding to $Re = 0$ according to our definition.[1] We can use these equilibrium simulations in order to identify differences among the various solid-wall boundary condition models. In Fig. 6 we plot the number density profiles extracted along the vertical (VV′) and diagonal (DD′) lines defined in Fig. 5. The results of simulations with FBC and ABC-0 are shown. The left plot in the figure shows that the use of FBC contributes to large density fluctuations in the near-wall region. However, density fluctuations can be smoothed out if we use the ABC-0 type. On the right plot we see that we have even

[1] We note that $Re = 0$ here does not correspond to Stokes flow, which is the typical notation.

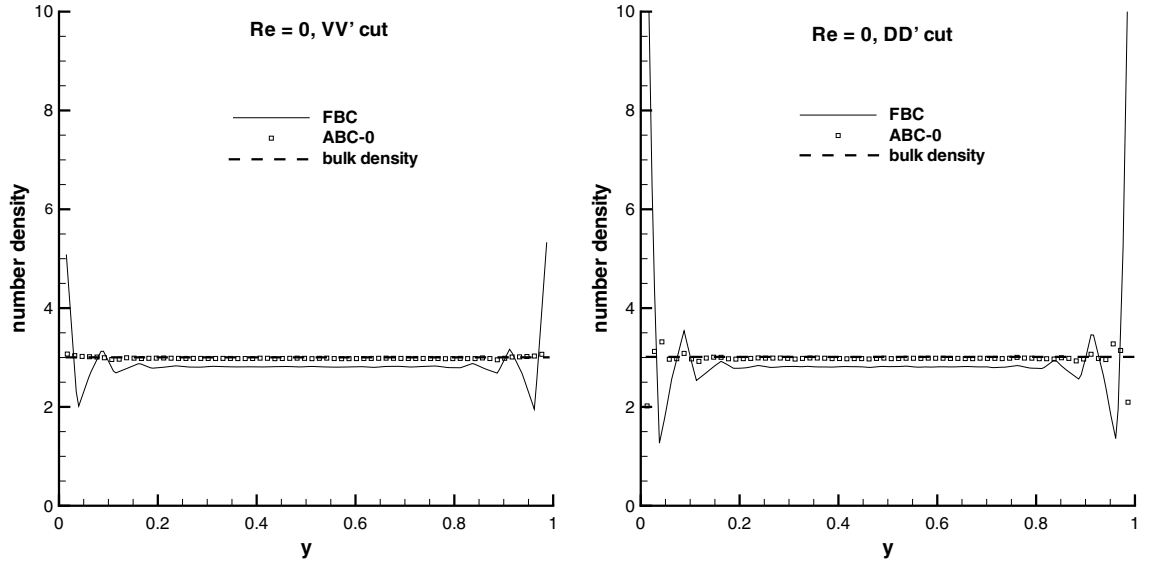

Fig. 6. Static fluid. Density profiles extracted along VV′ and DD′ lines. The y-coordinate is normalized by the domain size.

larger density fluctuations in the corners due to the presence of two intersecting walls. For ABC-0 and ABC-I we have a significant improvement of the number density in the corner. For EBC-0 and EBC-S types we find that the density profile is essentially uniform.

The static fluid simulations reveal the effect of applying different boundary conditions. In the following, we will identify one more effect when the fluid is in motion, namely *compressibility*. Therefore, it is important to consider in DPD simulations of wall-bounded flows the boundary condition effect on density fluctuations *separately*, and note that certain implementations may eliminate this effect while for other implementations strong boundary effects may be present.

We first performed DPD simulations in the regime of relatively small Reynolds numbers, i.e., $10 < Re < 50$, using different types of boundary conditions. In Fig. 7 we present simulation results for the flow at $Re = 25$. Results obtained by the spectral element method (SEM) are plotted with lines, and DPD results are shown with symbols. We have a very good agreement between the DPD and the continuum-based simulations, which

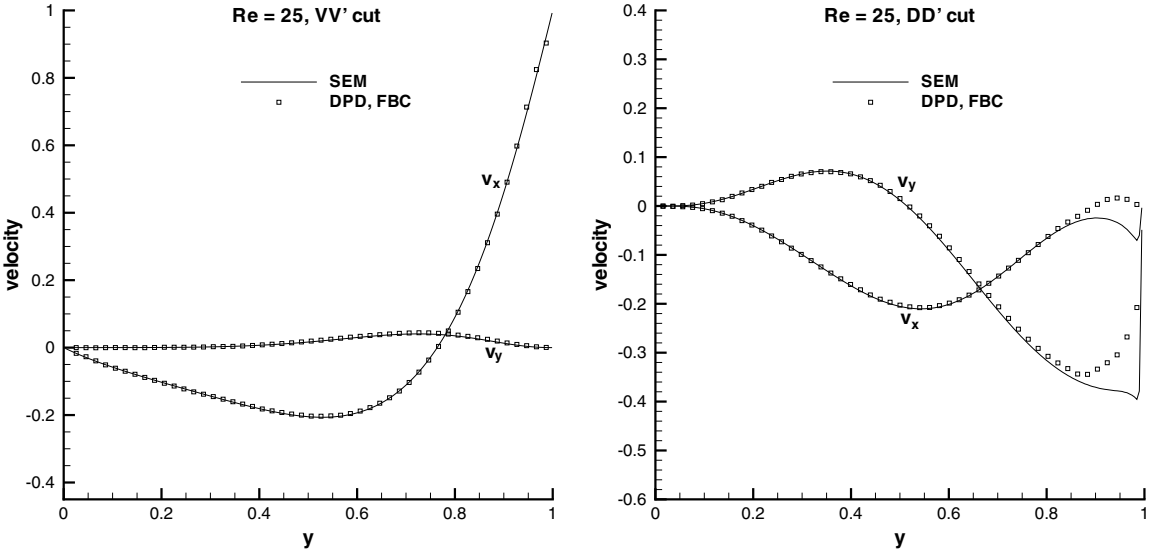

Fig. 7. Velocity profiles extracted along the VV′ and DD′ lines. $Re = 25$.

is typical in this range $Re \leqslant 50$. The discrepancy in the corner for the DD′ cut can be explained by the lack of DPD resolution there, where a very sharp velocity gradient is present. We also note that DPD can be used to accurately simulate flows in the range of low Reynolds numbers, i.e., $Re < 10$. However, computationally it can become very expensive to obtain a smooth solution because it requires a long-time averaging.

4.4. Moderate Reynolds number flow

Next we increase Reynolds number further but within the range $50 < Re < 400$, and find that the DPD results using FBC give a noticeable discrepancy compared to the spectral element results. In order to investigate the reasons for the DPD failure in this case we consider the fluid density fluctuations in the corner where the moving wall encounters the stationary vertical wall. Fig. 8 shows density profiles extracted along the DD′ line. This plot shows that at the corner $x = y = 1$ the maximum density increases with Re for the fixed computational domain (L is fixed) or equivalently with the velocity of the moving wall. This is due to compressibility effects allowing for a particle accumulation in the corner as the particles moving along the upper wall encounter an obstacle represented by the stationary vertical wall. We also note that approximately up to $Re = 50$ the density profile around the corner region remains similar to that of a static fluid, even though the maximum number density at the corner increases. For higher Reynolds numbers ($Re > 50$) the density profile in the corner starts changing drastically, and the local dense region grows in size and leads to modification of the global flow structure, and hence it affects the large vortex at the center of the cavity.

Next, we perform a series of DPD simulations using ABC-0 to model the wall boundaries. The new results show that the density fluctuations at the corner $x = y = 1$ are substantially reduced, hence the agreement of DPD results with the continuum-based solutions is valid in a wider range of Reynolds numbers, e.g., $0 < Re < 100$. Fig. 9 shows density profiles extracted along the DD′ line. As we also found in Poiseuille flow, ABC-0 improves the near-wall density fluctuations, and therefore density fluctuations are less pronounced compared to simulations employing FBC. Moreover, since we employ here the *standard* DPD method other boundary condition models (e.g., ABC-I, EBC-0, or EBC-S) have similar performance to ABC-0.

4.5. Effect of domain size

In order to simulate higher Re number flows we can increase the size of the computational domain. To this end, we performed several simulations for the cavity domain of size $20 \times 20 \times 500$. These results indicate that

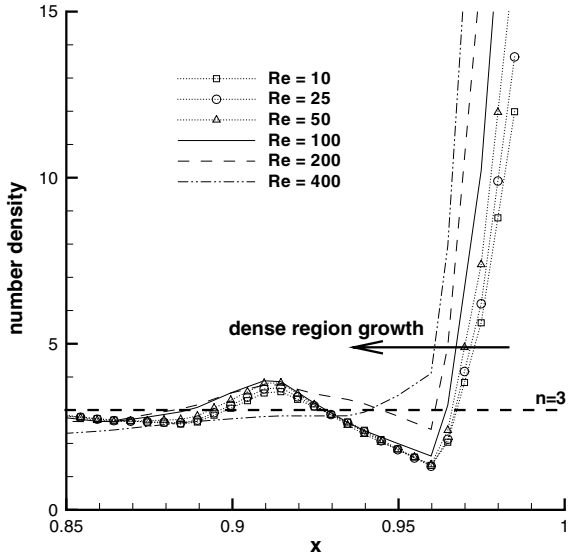

Fig. 8. Density profiles extracted along DD′ line for different Re. Force boundary condition (FBC). The coordinates are normalized by the domain size.

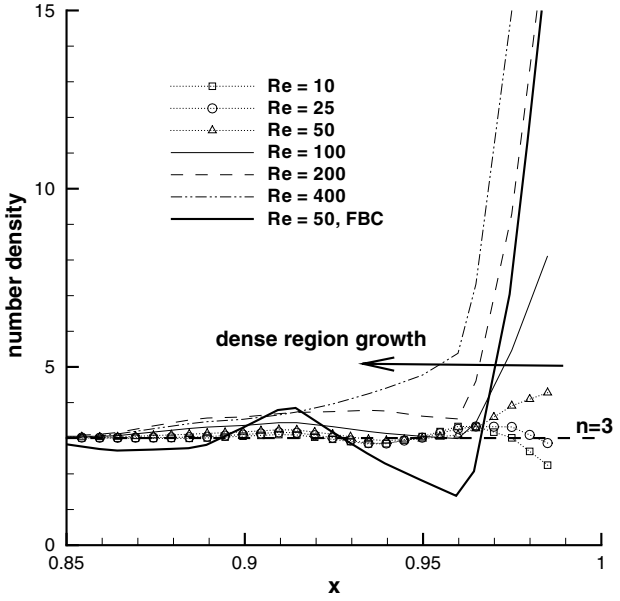

Fig. 9. Density profiles extracted along DD′ line for different *Re*. Adaptive boundary condition (ABC-0). The coordinates are normalized by the domain size.

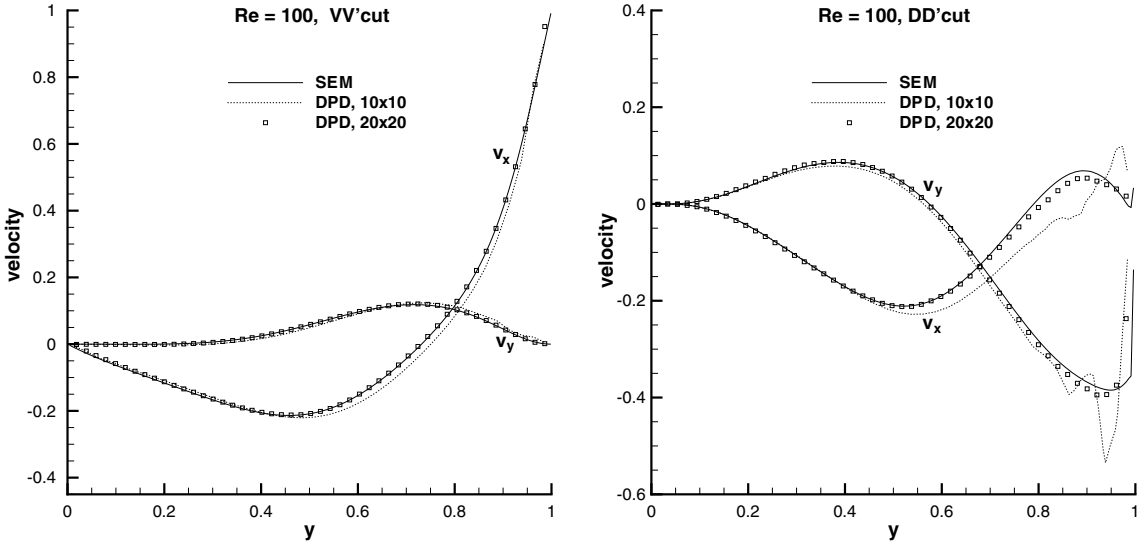

Fig. 10. Effect of domain size. Velocity profiles extracted along the VV′ and DD′ lines. The coordinates are normalized by the domain size. ($Re = 100$).

we can reach an accurate solution for Reynolds number twice as big compared to the 10×10 domain. A further analysis of this will be given below. In Fig. 10 we present typical simulation results for $Re = 100$ using FBC to model the walls for the 10×10 and 20×20 domains. We have already demonstrated that the domain 10×10 with FBC can be used to accurately simulate flows in the range $0 < Re < 50$. However, for the domain 20×20 with FBC we are able to use DPD for a somewhat wider range, i.e., $0 < Re < 100$, at comparable accuracy.

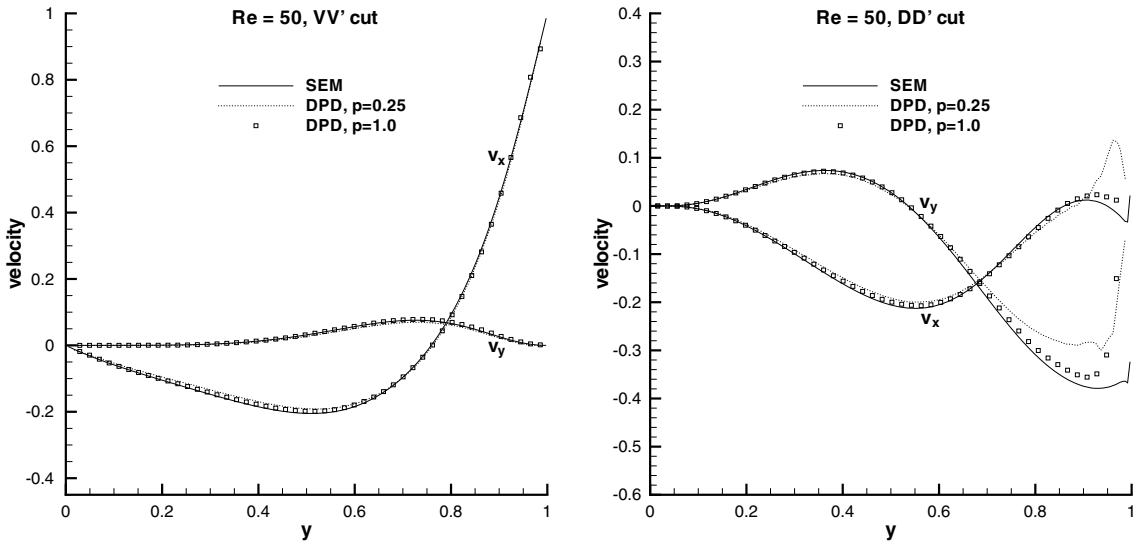

Fig. 11. Velocity profiles extracted along the VV′ and DD′ lines for standard ($p = 1$) and modified ($p = 0.25$) DPD methods. The coordinates are normalized by the domain size. ($Re = 50$).

4.6. Modified DPD

Here we study the performance of the modified DPD ($p = 0.25$ in Eq. (7)) [1] and compare it with the standard DPD ($p = 1$ in Eq. (7)). The kinematic viscosity in this case increases to 0.5407. All other DPD simulation parameters remain the same as before, and we only have to adjust the velocity of the moving wall in order to match the targeted value of the Reynolds number. Fig. 11 compares our simulation results for the cavity flow at $Re = 50$ using EBC-S for different exponents $p = 1.0$ (standard DPD) and $p = 0.25$ (modified DPD). We note that the results for $p = 0.25$ are not very accurate compared to the results for $p = 1.0$. This is due to the increase of viscosity of a fluid which requires us to set a higher velocity for the moving wall in order to achieve $Re = 50$. The compressibility effects depend only on the repulsive interactions and not on the strength of the thermostat, i.e. the exact form of the dissipative and random DPD forces. A conclusion which can be drawn from these tests is that *it is advantageous to use low viscosity in the DPD simulations instead of high velocity to achieve a certain Re value.* With regards to boundary conditions, we employed EBC-S type here based on the aforementioned results for channel flow, i.e., EBC-S performs well both for the standard and modified DPD version. In order to quantify the effect of different types of boundary conditions for the modified DPD method, we also run simulations using ABC-0. Fig. 12 shows corresponding results at $Re = 25$. The use of ABC-0 leads to larger errors in the solution as this type of boundary condition adjusts properly the repulsive forces but not the dissipative forces. We also note that ABC-I performs similarly to EBC-S but FBC and EBC-0 also lead to large errors, essentially confirming our initial conclusions based on the Poiseuille flow study in Section 3.

4.7. Number density effect

Groot and Warren have shown that a sufficiently high number density ($n > 2$) is required in DPD simulations in order to obtain a good approximation for the fluid obeying a quadratic equation of state [3]. They have also derived a formula which relates the dimensionless compressibility k^{-1} of the fluid to the number density, conservative force coefficient, and temperature as follows

$$k^{-1} = 1 + \frac{2\alpha a n}{k_B T} \quad (\alpha = 0.101). \tag{12}$$

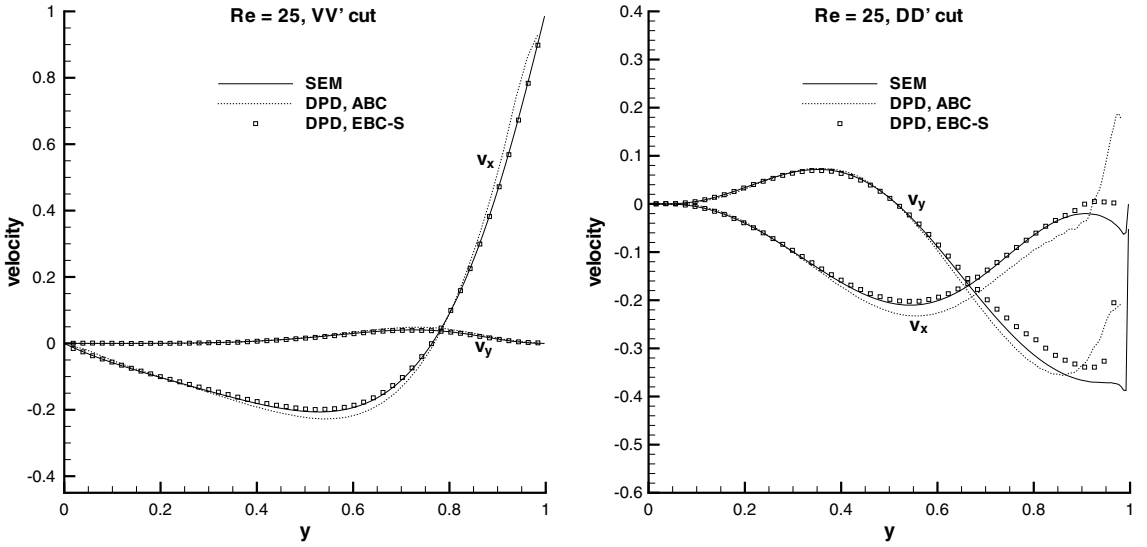

Fig. 12. Modified DPD: Velocity profiles extracted along the VV′ and DD′ lines for ABC-0 and EBC-S. The coordinates are normalized by the domain size. ($Re = 25$).

In principle, the number density chosen for the simulation is a free parameter, however, often the value $n = 3$ is used as a lowest possible density due to increasing computational cost for larger densities. Further, we investigate the issue of compressibility and boundary condition effects for the cavity flow utilizing different fluid number densities. We have performed a series of simulations for the cavity flow in the regime $0 < Re < 200$ using bulk number densities $n = 3$, 6 and 9 for the small domain size 10×10, and also bulk number densities $n = 3$ and 6 for the larger domain size 20×20. In all simulations we fix the dimensionless compressibility and temperature and adjust the conservative force coefficient to the bulk number density using Eq. (12). Specifically, we run simulations for three sets of those parameters: (1) $n = 3, a = 25$; (2) $n = 6, a = 12.5$; (3)

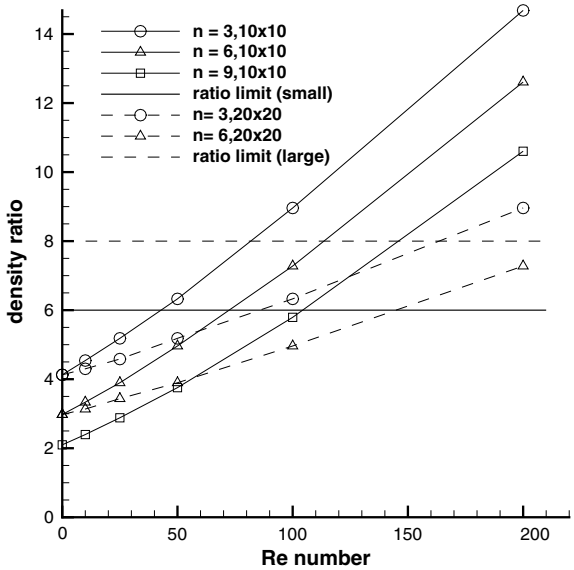

Fig. 13. Limit of DPD applicability: Plotted is the number density ratio $n_{\max}/n$ as a function of the Reynolds number Re. The solid lines are for the 10×10 domain while the dash lines are for the 20×20 domain. The $Re = 0$ case corresponds to the equilibrium state, i.e., static fluid. The walls are modeled using the FBC formulation.

$n = 9, a = 8.33$. We note that we maintain the same fluid dimensionless compressibility in order to be able to definitively separate the compressibility effects from the boundary condition effects.

The results presented so far suggest that the limit of DPD applicability can be determined by the maximum allowed velocity of the moving wall or alternatively by the maximum allowed number density in the corner. However, it appears that this limit can be well characterized by the density ratio $n_{\max}/n$ where $n_{\max}$ is the maximum density in the corner (averaged over the corner bin) and n is the bulk density. Fig. 13 shows the dependence of the density ratio on the Reynolds number for simulations in the small and large domains; each symbol in the plot corresponds to a separate cavity flow simulation.

An important finding is that the number density ratio varies approximately linearly with *Re*. Furthermore, the lines which correspond to different number densities are parallel, hence the density ratio has the same functional dependence for all bulk number densities, i.e. these lines have equal slopes. This, in turn, implies that the response of number density ratio to a change in *Re* (or equivalently to the velocity of the moving wall) is identical and independent of the bulk number density. This fact supports the idea that the limit of DPD applicability can be determined by a criterion which is independent of the specific value of the bulk number density used. The $Re = 0$ case corresponds to zero velocity of the upper wall, hence this is an equilibrium state. The deviation of the DPD solution from the expected accurate solution ($n_{\max}/n = 1$) for $Re = 0$ is due *solely* to the boundary condition implementation. In particular, the boundary conditions employed for the simulation results shown in Fig. 13 are of the FBC type. We see that as the bulk number density increases the effect of the boundary condition is less pronounced. Simulations with the other types of boundary conditions (i.e., ABC or EBC) give the expected solution at $Re = 0$, i.e., they intersect the vertical axis at $n_{\max}/n \approx 1$. At this point, we can separate the effects of boundary conditions from the compressibility effects, given the aforementioned parallel form of the number density lines. In particular, the contribution of the boundary conditions can be extracted from the $Re = 0$ case while the linear increase with *Re* in the maximum number density is *entirely* due to compressibility effects.

Our simulation results show that the limit of DPD applicability can be determined by the maximum allowed number density ratio, which is independent of the bulk number density but depends on the geometry and to some degree on the size of the bin selected for statistical averaging. For example for the cavity size 10×10 with 40×40 bins, we found that the maximum allowed number density ratio for the standard DPD method is approximately $n_{\max}/n = 6$, see horizontal solid line in the figure. (This value is obtained by systematic comparison of the velocity field from the DPD simulations with the reference spectral element solutions based on the incompressible Navier–Stokes equations.) The intersection of the horizontal line (defined by $n_{\max}/n = 6$) with the inclined lines determines the maximum *Re* that can be accurately simulated. This is demonstrated in Figs. 14 and 15, where we plot velocity profiles extracted along a vertical (VV′) and diagonal

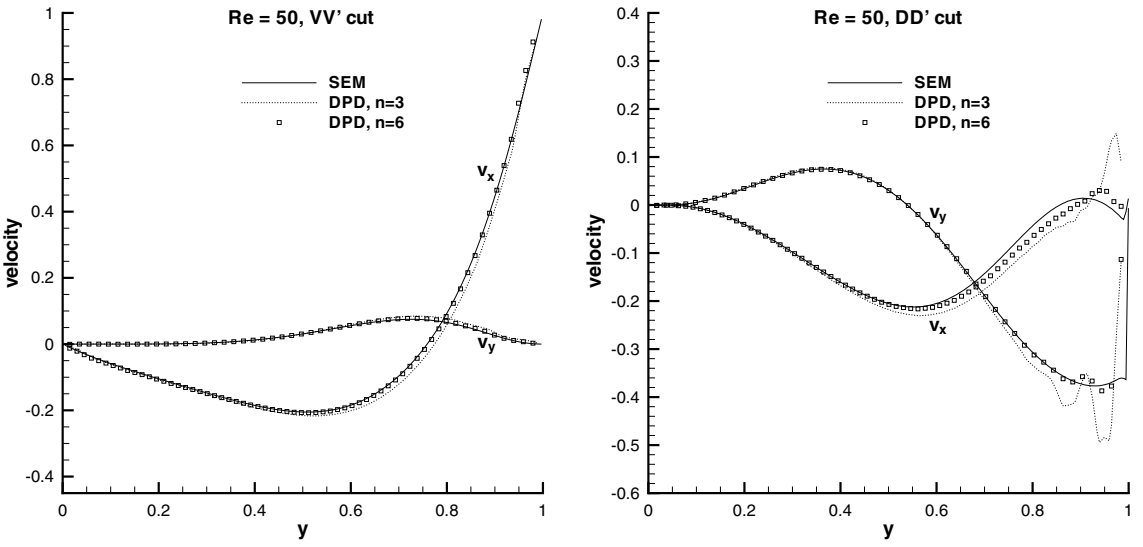

Fig. 14. Velocity profiles extracted along VV′ and DD′ lines for number density 3 and 6. ($Re = 50$; small domain).

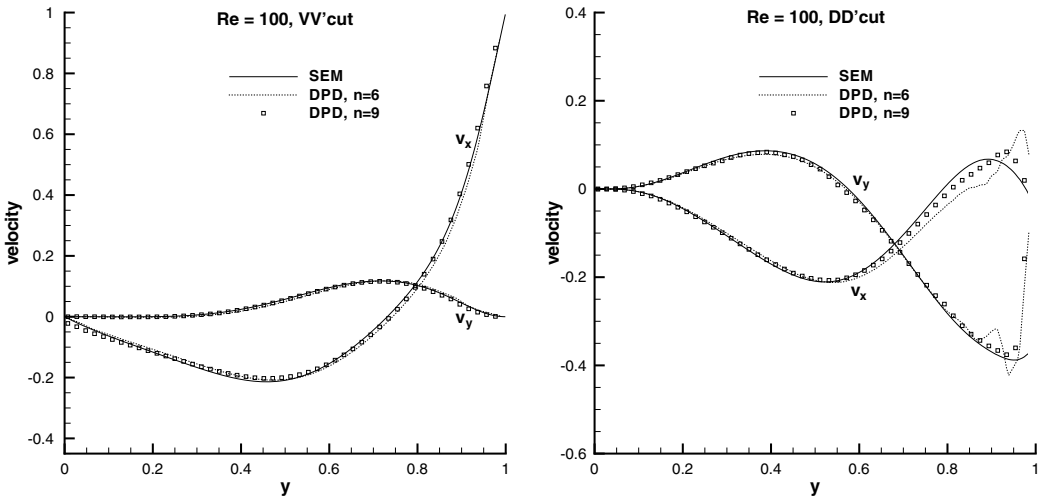

Fig. 15. Velocity profiles extracted along VV′ and DD′ lines for number density 6 and 9 ($Re = 100$; small domain).

(DD′) cuts for $Re = 50$ and $Re = 100$, respectively, employing different number densities in simulations. Although the results for the case $Re = 50$, $n = 6$ are in a good agreement with the spectral element solution, the case $Re = 50$, $n = 3$ shows a noticeable discrepancy in the results. We find a similar behavior in the case of $Re = 100$ for densities 6 and 9. Clearly, for selected domain size, $Re = 50$ and 100 are close to the maximum Reynolds number values that can be simulated at number density $n = 6$ and $n = 9$, respectively. We observe that higher number density allows one to simulate higher Re number flows with the FBC model. This is due to the fact that the boundary condition effects on the near-wall density fluctuations is weaker for higher number density flows.

In Fig. 13 we have included results from simulations in a larger cavity domain, and we observe that the slope of the lines corresponding to the 20×20 cavity is half that of the lines corresponding to 10×10 cavity. This is due to the fact that for the same Re the velocity of the horizontal wall is halved in the larger domain, and we have already seen the strong dependence of the accuracy of the DPD simulation on the wall's velocity magnitude. However, in order to determine the true limit in Re in the larger domain simulations, we have to consider the bin size employed in the statistical averaging. If we keep the same bin size as in 10×10 cavity we would have 80×80 bins and the DPD limit of $n_{\max}/n = 6$ is valid, independent of the bulk number density used. However, if we employ a 40×40 grid of bins then the size of the bin is twice larger than the bin size for the small domain, and, hence, the density fluctuations are reduced due to the wider area averaging. Using similar comparisons between the spectral element solutions and the DPD results processed on the large domain but with the 40×40 bin, we find that the limit of DPD applicability seems to be even higher, e.g., $n_{\max}/n \approx 8$. So in brief, these results show that two different criteria employed in the comparison of DPD with the spectral element results may lead to somewhat different values of the threshold ratio $n_{\max}/n$.

We can now use the findings we just discussed in order to collapse all the results plotted in Fig. 13 into a single "master" curve. In particular, if we repeat the previous simulations with the more accurate boundary conditions (ABC or EBC) there will be no dependence on the nominal value of the bulk density so all parallel curves collapse to a single curve passing through $n_{\max}/n = 1$ in the vertical axis (at $Re = 0$). Moreover, the slope of the curves depends on the wall's driving velocity, hence if we replace Re in the horizontal axis with the velocity of the wall U we should expect different domain sizes to also collapse onto one curve. This is, indeed, the case and the "universal" curve is shown in Fig. 16. In order to obtain the maximum value of velocity for which we obtain correct flow fields we propose, based on our results, an upper limit of $n_{\max}/n$ in the range $[5, 10]$ for all cases. To test this criterion we performed parallel simulations (on 512 Blue Gene processors) at a much higher $Re = 1000$ on a $100 \times 100 \times 10$ domain using EBC-S boundary conditions. Here, we keep all simulation parameters the same and set the velocity of the moving wall to 2.854 in order to match $Re = 1000$. (The case with velocity $v = 2.854$ corresponds approximately to the density ratio 5 in Fig. 16,

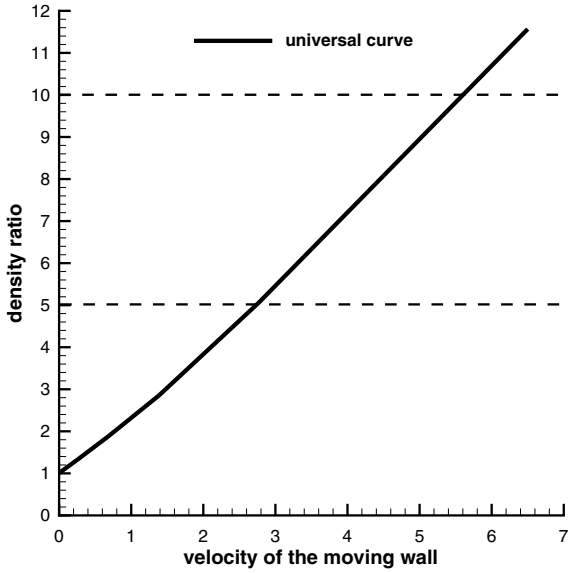

Fig. 16. Universal curve for the maximum number density ratio versus the driving velocity.

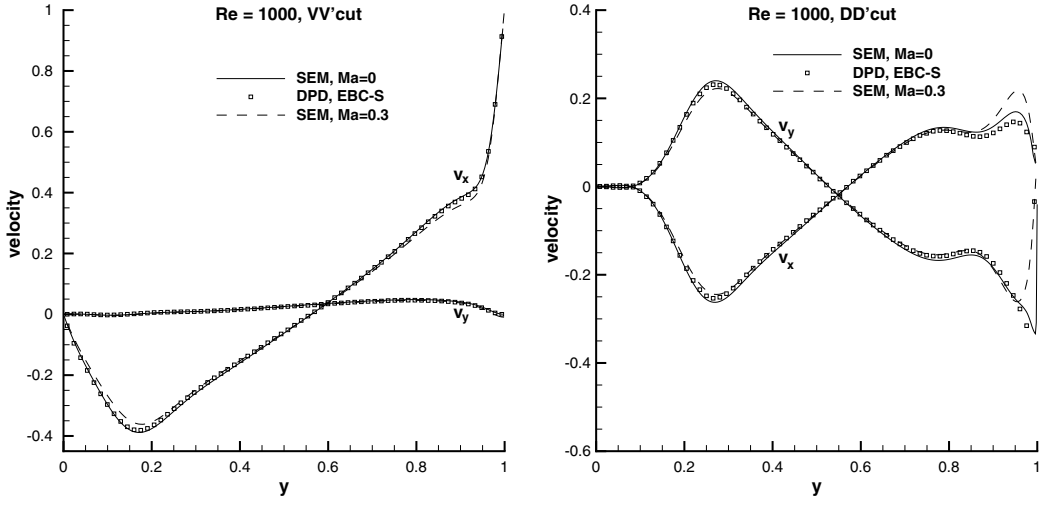

Fig. 17. Velocity profiles extracted along the VV′ and DD′ lines. $Re = 1000$.

and, therefore, the DPD simulation results are expected to be accurate.) In Fig. 17 we present simulation results at $Re = 1000$ including spectral element simulations of incompressible and compressible (at nominal Mach number 0.3) flows. To prove that DPD accurately captures the flow field structure in this relatively high Reynolds number case we present comparisons of the velocity field in terms of v_x and v_y contour plots in Fig. 18. In general, we observe a very good agreement of the DPD results with the spectral element solutions. In particular, the DPD contours seem to lie between the contours of the incompressible and compressible solutions.

We have also performed a similar simulation using the *modified* DPD, see Fig. 19. The velocity of the moving wall in this case is set to 5.407, which corresponds to approximately 9.5 value of the density ratio on the master curve. Here we see a more pronounced difference with the incompressible spectral element results, as expected in this case, due to the fact that compressibility effects become more important. We find that the modified DPD contours are closer to the compressible $Mach = 0.3$ solution, however there is a large discrepancy of the results in the corner. The $Re = 1000$ simulations verify that if the upper limit of $n_{\max}/n$ is in the

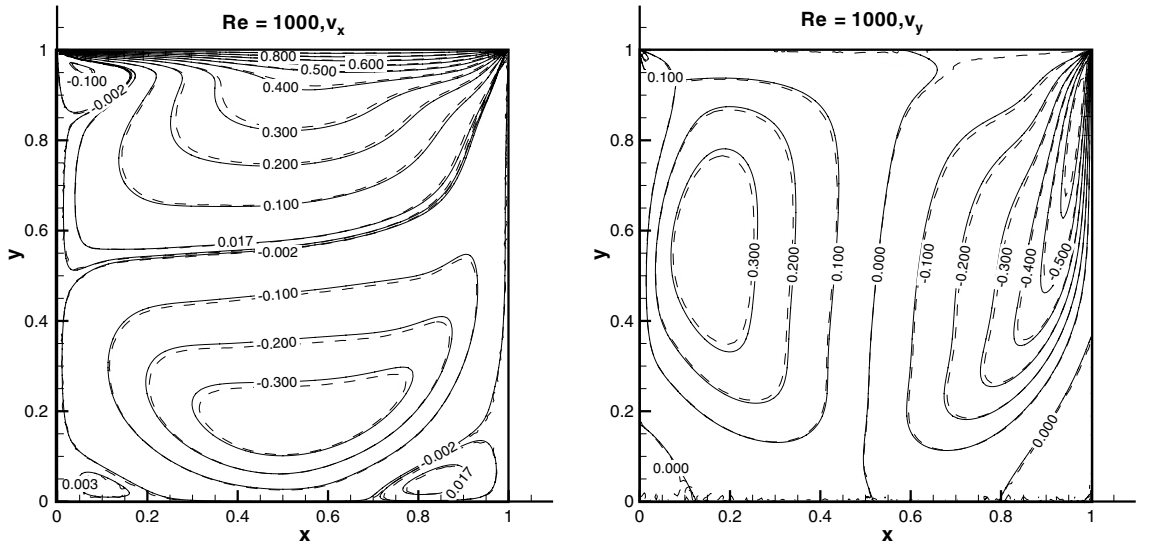

Fig. 18. Contours of v_x (left) and v_y (right). SEM incompressible results are denoted by solid lines, compressible solution ($Mach = 0.3$) by dotted lines and *standard* DPD results by dashed lines. $Re = 1000$.

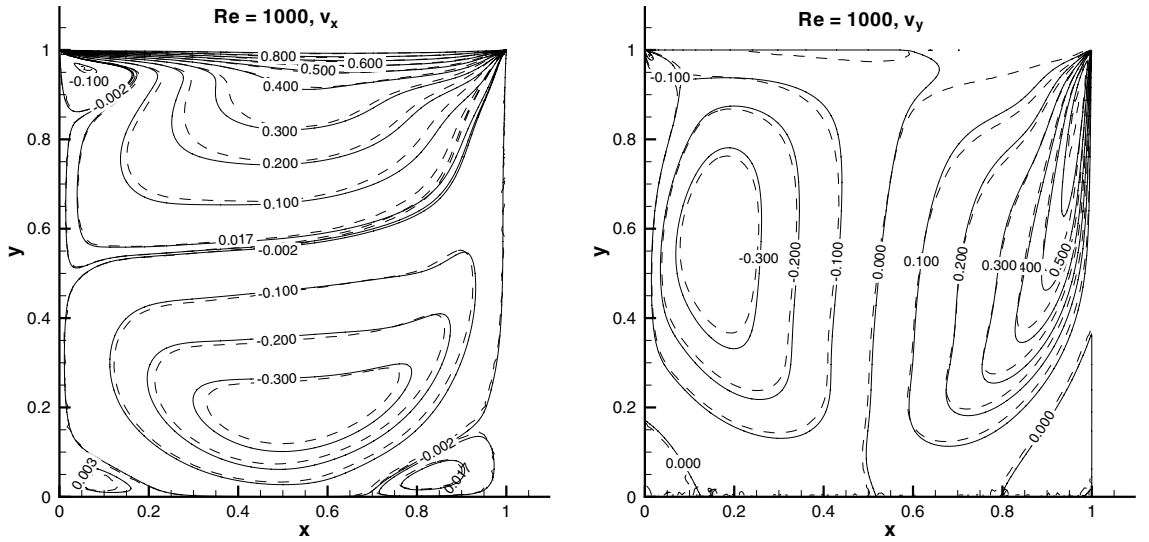

Fig. 19. Contours of v_x (left) and v_y (right). SEM incompressible results are denoted by solid lines, compressible solution ($Mach = 0.3$) by dotted lines and *modified* DPD results by dashed lines. $Re = 1000$.

range $[5, 10]$ the DPD results will be accurate. This limit can be used in selecting an appropriate domain size for the desired Re number flow simulation.

5. Summary

In this paper we have studied the two fundamental issues that limit the maximum Reynolds number that can be achieved in DPD simulations of wall-bounded flows, namely, *boundary conditions* and *compressibility effects*. In order to enforce accurately wall boundary conditions in DPD, we have to properly model the interaction forces between the wall and the fluid particles. Specifically, the *wall-normal* component of the conservative force controls the density fluctuations while the *wall-tangential* component of the dissipative force

enforces the correct velocity slope in the near-wall region. (The average random force is zero and does not play an important role in the correct imposition of boundary conditions.) The models ABC-I and EBC-S that we studied make the proper force adjustments for both components whereas FBC, ABC-0 and EBC-0 modify only the wall-normal conservative force component. The DPD simulations we presented here for Poiseuille flow as well as flow in a lid-driven cavity demonstrate that indeed ABC-I and EBC-S yield superior results. Density fluctuations around the bulk density in the case of the lid-driven cavity may achieve very large values at the corners formed between two intersecting walls. We have developed a simple criterion to diagnose erroneous DPD results based on the ratio of the maximum density in the domain over the bulk density; the upper limit of this ratio should be in the range [5, 10]. To achieve accurate DPD results at higher Reynold number, we propose to increase the size of the computational domain. Our criterion can be used to predict the minimum domain size to achieve a specific Reynolds number. We have demonstrated this by simulating accurately flow in the cavity at $Re = 1000$ using both the standard as well as a modified version of DPD, the latter associated with highly viscous fluids.

Increasing the domain size requires more DPD particles, so here we provide an approximate analysis of the associated *computational cost*. Specifically, the cost of DPD simulation per time-step is proportional to the number of particle pairs, since only pairwise interactions are involved in the computation. Hence, the cost of the simulation with the simplest implementation would be proportional to N^2, where N is the number of particles in the simulation. However, the forces in DPD act locally within the cutoff radius r_c, and, hence, a more effective implementation is to consider only neighboring pairs (N_n of them). Correspondingly, the cost per time-step is cost $\sim CN \times N_n$, where the constant C represents the number of operations required for each pair. We have verified this scaling in equilibrium simulations (periodic box domain) using different number of particles N, with results revealing that cost $\sim N^{1.1}$ if more than 10^4 particles are used. If we now increase the cavity domain size in x and y dimensions by k times the corresponding number of particles is k^2N while the number of bins is k^2N_b. The computational cost per time step is cost $\sim Ck^2N \times N_n$, so the simulation is k^2 times more expensive. However, we also need to account for an increase in the total number of time-steps required for the larger domains, namely: (i) the time t_s required to reach a statistically steady state; (ii) the time t_a required to perform the data averaging after the steady state is reached. To this end, we can estimate t_s from the diffusion limit, i.e., $t_s \propto L/\sqrt{\nu}$, while $t_a \sim N_{steps}\frac{N_b}{N}$ where N_{steps} is the number of steps required to reach the desired accuracy, and N_b is the number of bins used for statistical processing. Hence, to reach steady state in the larger domain requires an extra cost by a factor of k^3 but the statistical averaging cost is constant for comparable accuracy with the small domain.

Finally, we comment on the *generality* of our criterion and specifically how does it extend to other wall-bounded flows. To this end, we can examine if our criterion is valid for the triangular-cavity flow presented in the introduction, for which we have performed similar DPD simulations with different boundary condition models and at different Reynold number. The DPD results, using FBC, are in a good agreement with spectral element results for $Re < 30$. We encountered similar problems to the square-cavity case, i.e., density fluctuations in the near-wall region due to boundary conditions and compressibility effects. Analysis of DPD results at different number densities showed that the density ratio, which identifies DPD applicability is equal to 5 in this case. This limit is in the lower end of the interval [5, 10] which we proposed because the triangular-cavity has a sharper angle between moving and stationary wall boundaries, and this favors compressibility effects. The use of the more accurate boundary conditions widens the range of DPD applicability, similarly to the square-cavity flow. As it was noted before, we can simulate higher *Re* number flows by simply making the computational domain larger at approximately linear cost. With regards to external flows (e.g., flows past bluff bodies), our experience is that the problems we discussed in this paper are less pronounced for such flows, because convex type of geometries appear not to favor particle accumulation close to the boundary. However, there are also outstanding issues associated with DPD simulation of such flows, most notably the accurate imposition of inflow/outflow boundary conditions, a topic for future studies.

Acknowledgment

This work was supported by NSF grants IMAG and CI-TEAM. Simulations were performed on the NSF/SDSC Blue Gene system.

References

[1] X.J. Fan, N. Phan-Thien, S. Chen, X.H. Wu, T.Y. Ng, Simulating flow of DNA suspension using dissipative particle dynamics, Physics of Fluids 18 (6) (2006) 063102.
[2] P.J. Hoogerbrugge, J.M.V.A. Koelman, Simulating microscopic hydrodynamic phenomena with dissipative particle dynamics, Europhysics Letters 19 (3) (1992) 155–160.
[3] R.D. Groot, P.B. Warren, Dissipative particle dynamics: bridging the gap between atomistic and mesoscopic simulation, Journal of Chemical Physics 107 (11) (1997) 4423–4435.
[4] N.A. Spenley, Scaling laws for polymers in dissipative particle dynamics, Europhysics Letters 49 (4) (2000) 534–540.
[5] R.D. Groot, K.L. Rabone, Mesoscopic simulation of cell membrane damage, morphology change and rupture by nonionic surfactants, Biophysical Journal 81 (2) (2001) 725–736.
[6] A. Maiti, S. McGrother, Bead-bead interaction parameters in dissipative particle dynamics: relation to bead-size, solubility parameter, and surface tension, Journal of Chemical Physics 120 (3) (2004) 1594–1601.
[7] R. Ata, A. Soulaimani, A stabilized SPH method for inviscid shallow water flows, International Journal for Numerical Methods in Fluids 47 (2) (2005) 139–159.
[8] S. Succi, The Lattice Boltzmann Equation for Fluid Dynamics and Beyond, Oxford University Press, Oxford, 2001.
[9] A.J.C. Ladd, Numerical simulations of particulate suspensions via a discretized boltzmann equation. Part 1. Theoretical foundation, Journal of Fluid Mechanics 271 (1994) 285–309.
[10] P. Espanol, M. Revenga, Smoothed dissipative particle dynamics, Physical Review E 67 (2003) 026705.
[11] P. De Palma, P. Valentini, M. Napolitano, Dissipative particle dynamics simulation of a colloidal micropump, Physics of Fluids 18 (2006) 027103.
[12] J.M. Kim, R.J. Phillips, Dissipative particle dynamics simulation of flow around spheres and cylinders at finite Reynolds numbers, Chemical Engineering Science 59 (20) (2004) 4155–4168.
[13] S.M. Willemsen, H.C.J. Hoefsloot, P.D. Iedema, No-slip boundary condition in dissipative particle dynamics, International Journal of Modern Physics C 11 (5) (2000) 881–890.
[14] X.J. Fan, N. Phan-Thien, N.T. Yong, X.H. Wu, D. Xu, Microchannel flow of a macromolecular suspension, Physics of Fluids 15 (1) (2003) 11–21.
[15] I.V. Pivkin, G.E. Karniadakis, A new method to impose no-slip boundary conditions in dissipative particle dynamics, Journal of Computational Physics 207 (1) (2005) 114–128.
[16] E.E. Keaveny, I.V. Pivkin, M. Maxey, G.E. Karniadakis, A comparative study between dissipative particle dynamics and molecular dynamics for simple- and complex-geometry flows, Journal of Chemical Physics 123 (2005) 104107.
[17] G.E. Karniadakis, S.J. Sherwin, Spectral/hp Element Methods for CFD, Oxford University Press, Oxford, 2005.
[18] V. Symeonidis, B. Caswell, G.E. Karniadakis, Schmidt number effects in dissipative particle dynamics simulation of polymers, Journal of Chemical Physics 125 (2006) 184902.
[19] P. Espanol, P. Warren, Statistical-mechanics of dissipative particle dynamics, Europhysics Letters 30 (4) (1995) 191–196.
[20] I. Pagonabarraga, M.H.J. Hagen, D. Frenkel, Self-consistent dissipative particle dynamics algorithm, Europhysics Letters 42 (4) (1998) 377–382.
[21] A.W. Lees, S.F. Edwards, The computer study of transport processes under extreme conditions, Journal of Physics C 5 (1972) 1921–1927.
[22] J.A. Backer, C.P. Lowe, H.C.J. Hoefsloot, P.D. Iedema, Poiseuille flow to measure the viscosity of particle model fluids, Journal of Chemical Physics 122 (15) (2005) 154503.
[23] P. Malfreyt, D.J. Tildesley, Dissipative particle dynamics simulations of grafted polymer chains between two walls, Langmuir 16 (2000) 4732–4740.
[24] M. Revenga, I. Zuniga, P. Espanol, I. Pagonabarraga, Boundary models in DPD, International Journal of Modern Physics C 9 (8) (1998) 1319–1328.
[25] M. Revenga, I. Zuniga, P. Espanol, Boundary conditions in dissipative particle dynamics, Computer Physics Communications 122 (1999) 309–311.
[26] I.V. Pivkin, G.E. Karniadakis, Controlling density fluctuations in wall-bounded DPD systems, Physical Review Letters 96 (2005) 206001.
[27] T. Werder, J.H. Walther, P. Koumoutsakos, Hybrid atomistic-continuum method for the simulation of dense fluid flows, Journal of Computational Physics 205 (1) (2005) 373–390.